Publications of the Astronomical Society of the Pacific, 134:104101 (9pp), 2022 October https://doi.org/10.1088/1538-3873/ac98e0

Variability and Spectral Behavior of Gamma-Ray Flares of 3C 279

Gege Wang[1,2,4], Junhui Fan[1,2,4], Hubing Xiao[3,4], and Jinting Cai[1,2]
[1] Center for Astrophysics, Guangzhou University, Guangzhou 510006, People's Republic of China; wanggege@gzhu.edu.cn, fjh@gzhu.edu.cn
[2] Astronomy Science and Technology Research Laboratory of Department of Education of Guangdong Province, Guangzhou 510006, People's Republic of China
[3] Shanghai Key Lab for Astrophysics, Shanghai Normal University, Shanghai, 200234, People's Republic of China; hubing.xiao@shnu.edu.cn

Received 2022 August 22; accepted 2022 October 6; published 2022 October 25

Abstract

3C 279 showed enhanced flux variations in Fermi-LAT γ-ray observations from 2018 January to June. We present a detailed Fermi-LAT analysis to investigate the variability and spectral behaviors of 3C 279 during the γ-ray flares in 2018. In this work, we analyzed the γ-ray spectra and found that the spectra in either the flaring or quiescent states do not show any clear breaks (or cutoffs). This indicates that the dissipation region is outside the broad-line region, and the energy dissipation may be due to the inverse Compton process of scattering the dust torus infrared photons, this result is also consistent with that in Tolamatti et al. An external inverse Compton scattering of dusty torus (DT) photons is employed to calculate the broadband spectral energy distribution (SED). This model was further supported by the fact that we found flare decay timescale was consistent with the cooling time of relativistic electrons through DT photons. During the SED modeling, a relatively harder spectrum for the electron energy distribution is found and suggests these electrons may not be accelerated by the shock that happened in the dissipation region. Besides, the magnetic reconnection is also ruled out due to a low magnetization ratio. Thus, we suggest an injection of higher-energy electrons from outside the blob and raising the flare.

Unified Astronomy Thesaurus concepts: Active galaxies (17); Gamma-rays (637); Galaxy jets (601); Quasars (1319)

1. Introduction

It has been well established that blazars are the dominant γ-ray sources in the extragalactic sky (Ackermann et al. 2015; Ajello et al. 2020). Blazars have a jet viewed under small angles closing to the line of sight. The jet orientation results in extreme observational properties, including multi-band rapid variations, high and variable polarization, strong and variable γ-ray emissions, and apparent superluminal motion, which are believed to be associated with a relativistic beaming effect (Wills et al. 1992; Urry & Padovani 1995; Fan 2002; Villata et al. 2006; Fan et al. 2014, 2021; Xiao et al. 2015, 2019; Gupta et al. 2016; Abdollahi et al. 2020; Yang et al. 2022).

Emission from the blazar jet dominates nearly over the entire electromagnetic spectrum and forms a two-bump structure spectral energy distribution (SED). The lower energy bump is attributed to the synchrotron radiation of relativistic electrons. The higher energy bump is attributed to the inverse Compton (IC) scattering, which is further divided into synchrotron-self Compton (SSC) if the soft photons come from the synchrotron process and external Compton (EC) if the soft photons come from external photon fields, e.g., the accretion disk (Dermer & Schlickeiser 1993), the broad-line region (BLR) (Sikora et al. 1994; Fan et al. 2006), and the dusty torus (DT) (Błażejowski et al. 2000; Arbeiter et al. 2002; Sokolov & Marscher 2005) in the frame of leptonic scenario.

3C 279 is a FSRQ with a black hole mass of $(3-8) \times 10^8 M_\odot$ (Nilsson et al. 2009) located at a redshift $z \sim 0.536$ (Lynds et al. 1965). It is known to be one of the bright and powerful γ-ray sources in the high-energy sky. 3C 279 was the first blazar showing strong and rapid variability at GeV energies detected by EGRET onboard Compton Gamma Ray Observatory (CGRO) (Hartman et al. 1992), also the first FSRQ detected above 100 GeV (MAGIC Collaboration et al. 2008). Since the launch of Fermi-LAT in 2008 June, the all-sky monitoring capability of the Fermi-LAT has provided us with a continuous γ-ray flux investigation of 3C 279 for over 10 yr. 3C 279 showed several outbursts in the past 10 yr, it went through a series of distinct flaring flux duration from 2013 December to 2014 April, hour-scale γ-ray flux variability was observed, with a maximum flux of $(6.54 \pm 0.30) \times 10^{-6}$ photons cm^{-2} s^{-1} on 2014 April 3 (Paliya et al. 2015). On 2015 June 16, LAT observed a giant outburst from 3C 279 with a peak > 100 MeV flux of $\sim 3.6 \times 10^{-5}$ photons cm^{-2} s^{-1} averaged over orbital period intervals, with flux doubling time less than 5 minutes observed in its 2 minutes binned light curve (Ackermann et al. 2016). It is the second FSRQ type blazar reported after PKS 1222+216 with a similar short minute timescale flux variation (Aleksić et al. 2011). These studies provided constraints on the

---

[4] Authors to whom any correspondence should be addressed.

physical properties of the γ-ray emission region and emission processes (Hayashida et al. 2015; Paliya et al. 2015).

In 2018, 3C 279 became very active again with fluxes exceeding the previous 2015 level. Several studies have been carried out, mainly focusing on the correlation between multi-wave bands with hour binned light curves (Shah et al. 2019; Prince 2020; Goyal & Soida 2022). Shukla & Mannheim (2020) analyzed the minute timescale peak-in-peak variability and proposed that the particle acceleration is due to relativistic magnetic reconnection. However, the magnetic reconnection mechanism for the particle acceleration has been questioned for the reason of a low magnetization (Hu et al. 2020, 2021; Tolamatti et al. 2022), and the shock-in-jet model for the particle acceleration is considered for the 2018 flare (Tolamatti et al. 2022).

In the present work, we analyzed the LAT data in detail for the variability and spectral behaviors of 3C 279 during the γ-ray flares in 2018. Our measured γ-ray flux in 1 hr bins reached $\sim 4.5 \times 10^{-5}$ photons cm^{-2} s^{-1} on 2018 April 19, and the source flux variability was resolved down to 2 minutes binned timescales, allowing an investigation of variability on minute timescales. The paper is organized as follows: In Section 2 we outline the Fermi-LAT observations and the data analysis procedures. Following this, we calculate the broadband SED to investigate the main cause of the flux peak. We present the results of the discussion in the location of the γ-ray dissipation region and the jet kinematics during the flare in Section 3, and a summary is given in Section 4.

2. Fermi-LAT Gamma-Ray Light Curve and Spectra Analysis

2.1. Data Analysis

LAT scans the whole sky every three hours in the energy range from 20 MeV to >300 GeV (Atwood et al. 2009). We selected LAT data from the Fermi Pass 8 database in the time period from 2008 August 4 15:43:36 (UTC) to 2020 November 25 23:41:00 (UTC), with energy range in 0.1–300 GeV. Following the recommendations of the LAT team,[5] we selected events with zenith angles less than 90 deg to prevent possible contamination from the Earth's limb. The LAT science tool Fermitools 2.0.8 and instrument response function (IRF) P8R3_SOURCE_V2 were used. For the target 3C 279, a $20^\circ \times 20^\circ$ square region of interest (ROI) centered at its position given in 4FGL-DR2 (Abdollahi et al. 2020) was selected. The normalization parameters and spectral indices of the sources within 5 deg from 3C 279, as well as sources within the ROI with variable index $\geqslant 72.44$ (Acero et al. 2015), were set as free parameters. All other parameters were fixed at their catalog values in 4FGL-DR2. We used the original spectral models in 4FGL-DR2 for the sources in the source model. Gamma-ray spectra and lightcurves binned by hour and minute timescales in Section 2.3 were derived by an unbinned maximum likelihood analysis with `gtlike`. Galactic and extragalactic diffuse emission models were added to the source model using the spectral model file gll_iem_v07.fits and iso_P8R3_SOURCE_V2_v1.txt,[6] respectively. The normalizations of the two diffuse emission components were set as free parameters in the analysis.

2.2. Long-term Light Curve

We made the long-term light curve of the whole analysis time period above 100 MeV and found three obvious flares in 2018 in addition to the flare in 2015 June. Then we used the parameters in Section 2.1 and a simple power law for 3C 279 in the source model. We constructed light curves in the daily time bin from MJD 58091 to MJD 58373 by performing a standard binned maximum likelihood analysis. The daily binned light curve is shown in Figure 1, in which when flux data points have the maximum likelihood Test Statistic (TS) values larger than 9 were plotted. The observed gap in Figure 1 is due to a technical issue encountered on 2018 March 16 by Fermi spacecraft. LAT did not carry out any observations between 2018 March 16 and 2018 April 8.

2.3. Minute-scale Flare

In order to investigate the fast flux variability in detail, we constructed light curves in hour timescale bins (Figure 2(a)), in which when flux data points have TS values larger than 9 were plotted. We noted that the flare F1 and F3 did not show noteworthy fast component or profile, therefore, we only made minute timescale binned light curve for F2 (Figure 2(b)). The measured γ-ray flux in 1 hr bins reached $\sim 4.5 \times 10^{-5}$ photons cm^{-2} s^{-1} on 2018 April 19. Here we defined the flare period of F2 to be between MJD 58227.875 and MJD 58228.500 (2018 April 19 21:00:00 and 2018 April 20 12:00:00), as indicated in Figure 2(a). And it concludes 10 bins designated Stage "A" through "J," respectively. We fitted a constant value to each stage in F2 for both time bins, and calculated a probability (p-value) from χ^2 for each stage. While stage D, H, I resulted in p-values consistent with constant fluxes, we found significant indications of rapid variability on a minute timescale in the 2 minutes binned light curve. For stage B: $(p,\ \chi^2/\mathrm{dof}) = (1.789 \times 10^{-15},\ 87.11/8)$, stage C: $(p,\ \chi^2/\mathrm{dof}) = (3.370 \times 10^{-05},\ 47.24/15)$, stage E: $(p,\ \chi^2/\mathrm{dof}) = (1.747 \times 10^{-05},\ 31.85/6)$, stage F: $(p,\ \chi^2/\mathrm{dof}) = (2.145 \times 10^{-08},\ 51.45/8)$, stage G: $(p,\ \chi^2/\mathrm{dof}) = (0.013,\ 20.97/9)$.

We constructed light curves in 2, 3, and 5 minutes bins for the whole flare period of F2, and eventually found minute-scale flare profile only in stage B, which was shown in Figure 2(b).

---

[5] https://fermi.gsfc.nasa.gov/ssc/data/analysis/scitools/

[6] https://fermi.gsfc.nasa.gov/ssc/data/access/lat/BackgroundModels.html

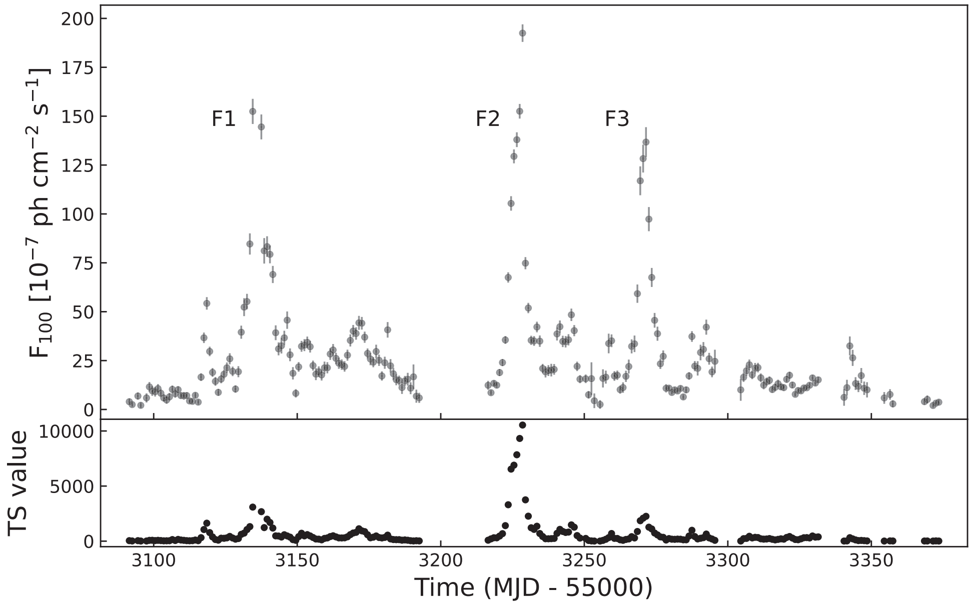

Figure 1. Long-term LAT light curve and three pronounced γ-ray flares (F1, F2, F3) during MJD 58091 to MJD 58373 from 3C 279 with daily time bin in the energy range of 0.1–300 GeV.

Then we used an exponential equation to fit the 2 minutes binned light curve profile, which is given by

$$F(t) = F_c + F_0(e^{(t_0-t)/T_r} + e^{(t-t0)/T_d})^{-1}, \tag{1}$$

where F_c and F_0 are the constant flux and height of a peak, respectively, t_0 is the flux peak time, T_r and T_d are used to measure the rise and decay time separately. The best fitting result gives $\chi^2/\mathrm{dof} = 1.71/5$ with the flare peak time t_0 on 26.16 (2018 April 19 22:16:10(UTC)). Flare peak flux with the best fitting at t_0 is $F_p = 4.32 \times 10^{-5}$ photons cm^{-2} s^{-1}. We calculate the average flux value of the four data points before flare as the flux in quiescence ($F_q = 1.90 \times 10^{-5}$ photons cm^{-2} s^{-1}), which is shown in Figure 2(b). The time when the flux equals to F_q before and after the flare is 15.66 and 50.99, respectively. Therefore the flux decay time (from F_p to F_q) is 24.83 minutes. We calculate the upper limit of F_c from the best fitting result of the exponential equation and take it as F_q, which equals to 2.25×10^{-5} photons cm^{-2} s^{-1}. Then we can get that the lower limit of flux decay time is 15.04 minutes.

2.4. The γ-Ray Spectral Analysis

We fit the γ-ray spectra of 3C 279 described with a log-parabola model ($dN/dE \propto (E/E_0)^{-\alpha-\beta\log(E/E_0)}$, where α and β are spectral parameters, here $E_0 = 466$ MeV). We plotted the spectral data points with TS > 4 and upper limits when TS < 4 in Figure 3. Figure 3(a) shows the spectra in the "*pre-outburst*" and "*post-flare*" periods as defined in Figure 2 for comparison. Figure 3(b) shows the γ-ray spectra as measured by Fermi-LAT for each stage. Stages B and C, and stages D, E, and F, were combined because they showed similar fluxes and spectral fitting results. The spectral energy flux peaks in each stage correspond with the light curve during the flare F2. The flux and spectral fitting results above 100 MeV for Each stage (A–J) during flare F2 are shown in Table 1.

The γ-ray flux (0.1–300 GeV) versus the γ-ray power law photon index Γ of 3C 279 with daily time bin based on the LAT data during the flare F2 is given in Figure 4. A correlation between the γ-ray flux and photon index was visible to suggest a "harder-when-brighter (BWB)" trend. The tendency of spectral hardening during the flaring state was seen in blazar flares by many authors (e.g., Britto et al. 2016; Shukla et al. 2018; Shah et al. 2019). A similar trend pattern was also previously seen for 3C 279 by Hayashida et al. (2015), Paliya et al. (2015) and Prince (2020). The BWB could be explained in many ways, such as two-component (one stable component and a variable one) model (Fiorucci et al. 2004), fresh electrons injection (Kirk et al. 1998; Mastichiadis & Kirk 2002), etc.

3. Discussion

3.1. The Location of the Dissipation Region

The question of the location of the blazar γ-ray dissipation region (d_{diss}) is intriguing to researchers. To directly determine the γ-ray location, we need an extremely large γ-ray telescope to fulfill the required resolution at its wavelength. Some indirect methods have been proposed to solve this issue, one of the popular ways is to measure the variability timescale and calculate the size of the dissipation

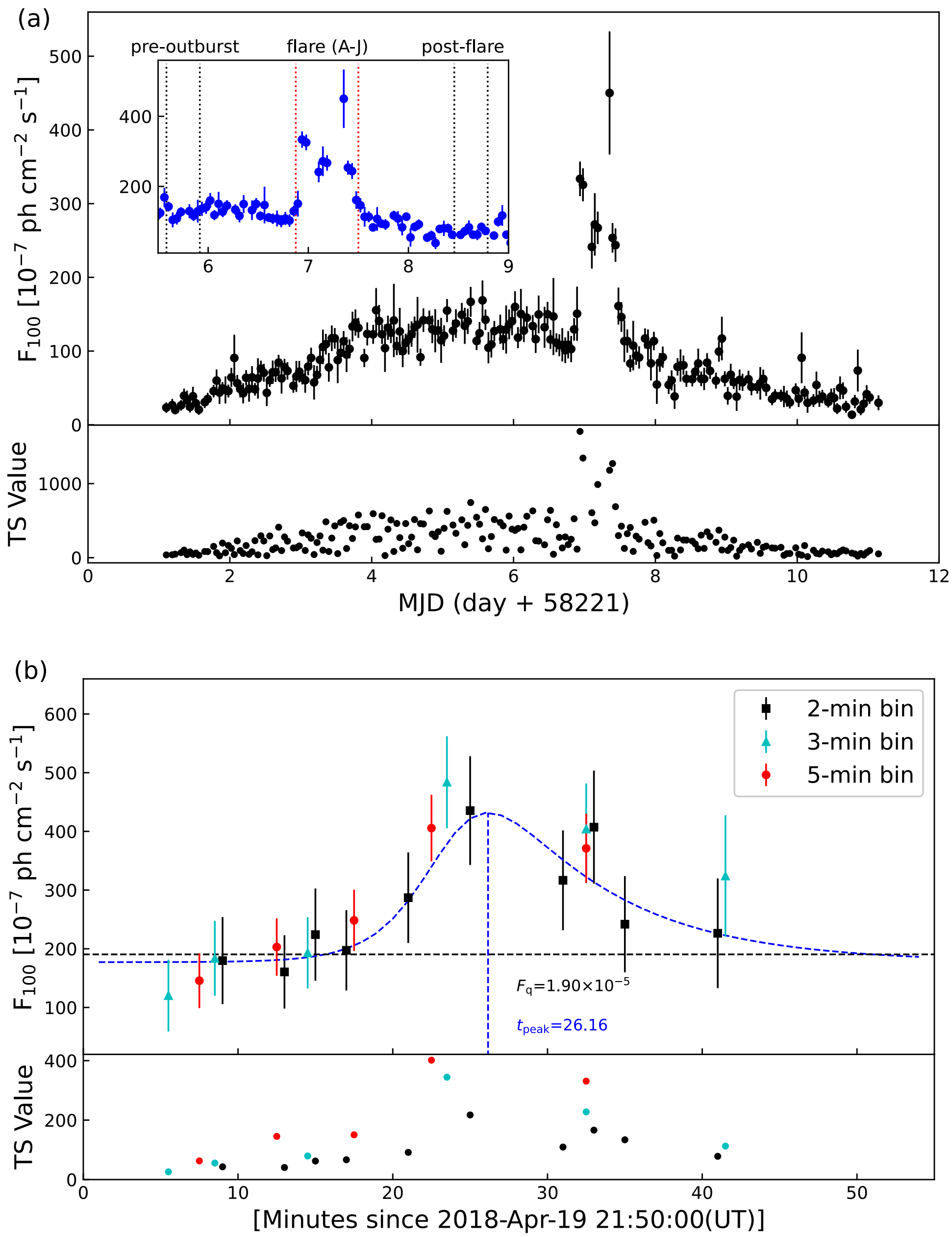

Figure 2. (a) Shows 1 hr binned light curve during flare F2 of 3C 279 above 100 MeV. Blue points in the upper left panel show the enlarged view of the peak-in-peak variability. And we selected 10 bins as the flare period designated Stage "A" through "J," respectively. (b) Shows the 2 minutes (black square), 3 minutes (cyan triangle) and 5 minutes (red point) binned light curves measured during stage B of flare F2 wherein a strong rapid minute-scale variability was observed. During stage B, 3C 279 was found to be highly inconsistent with the constant flux having p-value 1.789×10^{-15} (χ^2-test) for the two-minute binned light curve. The best-fit function to the 2 minutes binned light curve is deduced using an exponential equation represented by the dashed blue curve. The black dashed line shows the flux in quiescence.

region ($R_{\rm diss}$) by assuming the variability timescale accounts for the light travel across the dissipation region. Timescale from hours to minutes have been reported for blazars (Abdo et al. 2011; Tanaka et al. 2011; Brown 2013; Shukla et al. 2018) that constrain a very compact dissipation region. Then, the size of the dissipation region is used to calculate distance to the central black hole through $d_{\rm diss} = R_{\rm diss}\psi$ with an assumption that the dissipation region diameter is identical to the width of the jet at this distance, where ψ is the semi-aperture opening angle of the jet (Dermer et al. 2009;

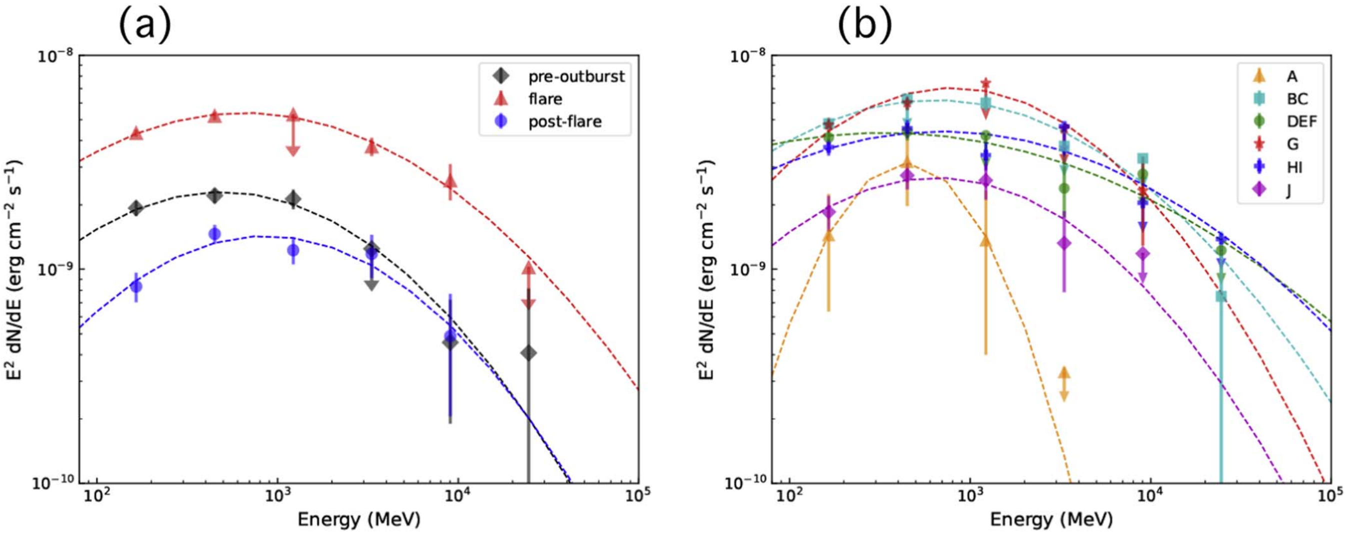

Figure 3. Gamma-ray spectra of 3C 279 for each stage during the flare F2, as well as "pre-outburst" and "post-flare" as indicated in Figure 2. The downward arrows represent 95% confidence level upper limits.

Table 1
Flux and Spectral Fitting Results of 3C 279 above 100 MeV for each Stage (A–J) during Flare F2

Stage Number	Epoch (MJD)	Flux ($\times 10^{-7}$)	α	β	TS
Pre-outburst	58226.58–58226.92	123 ± 19	1.98 ± 0.06	0.16 ± 0.03	2598
F2	58227.88–58228.50	270 ± 33	1.92 ± 0.03	0.12 ± 0.01	8156
Post-flare	58229.46–58229.79	67 ± 13	1.79 ± 0.12	0.17 ± 0.06	1451
A	58227.83–58227.92	151 ± 37	2.07 ± 0.10	0.78 ± 0.12	115
B–C	58227.92–58228.08	330 ± 23	1.92 ± 0.07	0.13 ± 0.03	2675
D–F	58228.08–58228.21	260 ± 31	2.04 ± 0.08	0.06 ± 0.03	1553
G	58228.21–58228.38	450 ± 43	1.80 ± 0.08	0.19 ± 0.04	1780
H–I	58228.38–58228.46	249 ± 21	1.93 ± 0.13	0.09 ± 0.05	1612
J	58228.46–58228.54	161 ± 25	1.89 ± 0.12	0.17 ± 0.07	298

Ghisellini & Tavecchio 2009). However, the distance is usually constrained to the base of the jet, where locates on the inner side of BLR, according to this method. The BLR is full of optical/UV photons, which will cause absorption to the high energy γ-ray photons through pair production ($\gamma\gamma \to e^{\pm}$) (Poutanen & Stern 2010) that arises a spectral cut-off at GeV energies. Acharyya et al. (2021) studied the γ-ray spectra for 18 flares and found that 11 of them with very high energy emission are incompatible with a BLR origin.

In the present work, we have studied the γ-ray spectra for the flare on 2018 April 19, see in Figure 3. Our results in Table 1 indicate that a log-parabola model is enough to fit the spectra and no significant cut-off at GeV energies is observed during the flaring state, suggesting the dissipation region is outside the BLR and the energy dissipation may be due to the IC process of scattering the DT infrared photons. This result is consistent with the one suggested by Tolamatti et al. (2022).

3.2. The Broadband SED Modeling

We calculate the broadband SED for "pre-outburst," "flare," and "post-flare" states of F2. We employ a log-parabolic-power-law (LPPL) function, which is a combination of a power-law function in the lower energy range and a log-parabola function at a higher energy range (Tramacere et al. 2009, 2011; Tramacere 2020), for the electron energy distribution (EED) in the dissipation blob (Massaro et al. 2006). The LPPL function is expressed as follows:

$$N(\gamma) = \begin{cases} N(\gamma/\gamma_0)^{-s}\ , \gamma \leqslant \gamma_0 \\ N(\gamma/\gamma_0)^{-(s+r\cdot\log(\gamma/\gamma_0))}\ , \gamma > \gamma_0, \end{cases} \tag{2}$$

where N is the normalization parameter, and γ_0 is the turn-over energy of the electron spectrum, s is the spectral index, and r is the spectral curvature.

In the framework of leptonic scenario (Ghisellini et al. 1996; Tavecchio et al. 1998), blazar broadband SED is formed through coupling the EED with the radiation

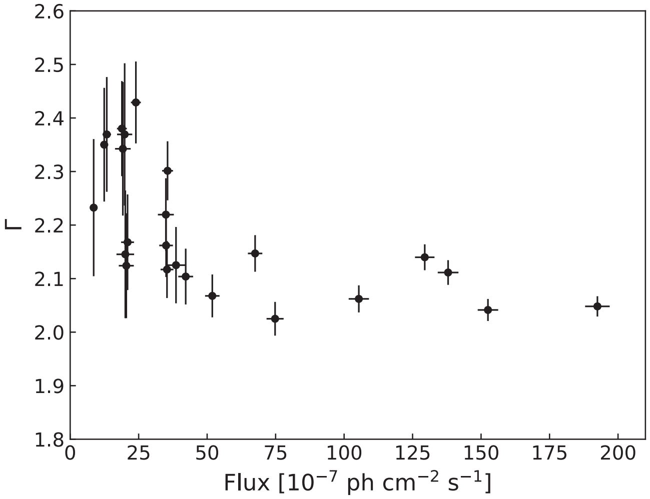

Figure 4. Scatter plot of the γ-ray flux (0.1–300 GeV) vs. the γ-ray power law photon index Γ of 3C 279 with daily time bin based on the LAT data during the flare F2.

mechanism (synchrotron radiation and inverse Compton scattering), and is usually displayed in the diagram of $\log \nu f_\nu - \log \nu$. In the present work, we introduce the *Jets SED modeler and fitting Tool* (*JetSet*)[7] (Tramacere et al. 2009, 2011; Tramacere 2020) to generate SEDs.

There are nine basic parameters to describe the SED model. Magnetic field (B), dissipation region size ($R_{\rm diss}$) and Doppler beaming factor (δ) to describe the dissipation region environment and the jet geometry. The rest of the six parameters, the maximum energy of electrons ($\gamma_{\rm max}$), the minimum energy of electrons ($\gamma_{\rm min}$), γ_0, N, s and r to describe the EED. In the case of FSRQs, the entire γ-ray emission is a combination of SSC, in which the soft photons are provided by the same population of relativistic electrons in synchrotron process, and external Compton scattering (EC), in which the soft photons can have multi-suppliers e.g., accretion disk (Dermer & Schlickeiser 1993), the broad emission line region (BLR) (Sikora et al. 1994; Fan et al. 2006), and the dusty torus (DT) (Błażejowski et al. 2000; Arbeiter et al. 2002; Sokolov & Marscher 2005).

We consider the EC model with soft photons origin from the DT, and there are 5 additional parameters to define the accretion disk and the DT, the disk luminosity ($L_{\rm disk}$), the disk temperature ($T_{\rm disk}$), the distance of the DT from the central engine ($R_{\rm DT}$), the temperature of the DT ($T_{\rm DT}$), and the opacity of the DT ($\tau_{\rm DT}$).

The simultaneously observed data that we used for SED calculation are collected from Tolamatti et al. (2022), in which the multi-wavelength data of duration MJD 58218–58243 is concluded. This duration spans 25 days and has a full coverage of flare F2. Thus, we collect radio, optical/UV, and X-ray data from their work to combine with our GeV γ-ray data of the three states. Here we show the SED fitting results of the three states of F2 in Figure 5. During the SED fitting, we have six parameters fixed as tabulated in Table 2 and the rest seven parameters to vary in Table 3, and the quantities related to jet power and SED structure for all the three states are listed in Table 4.

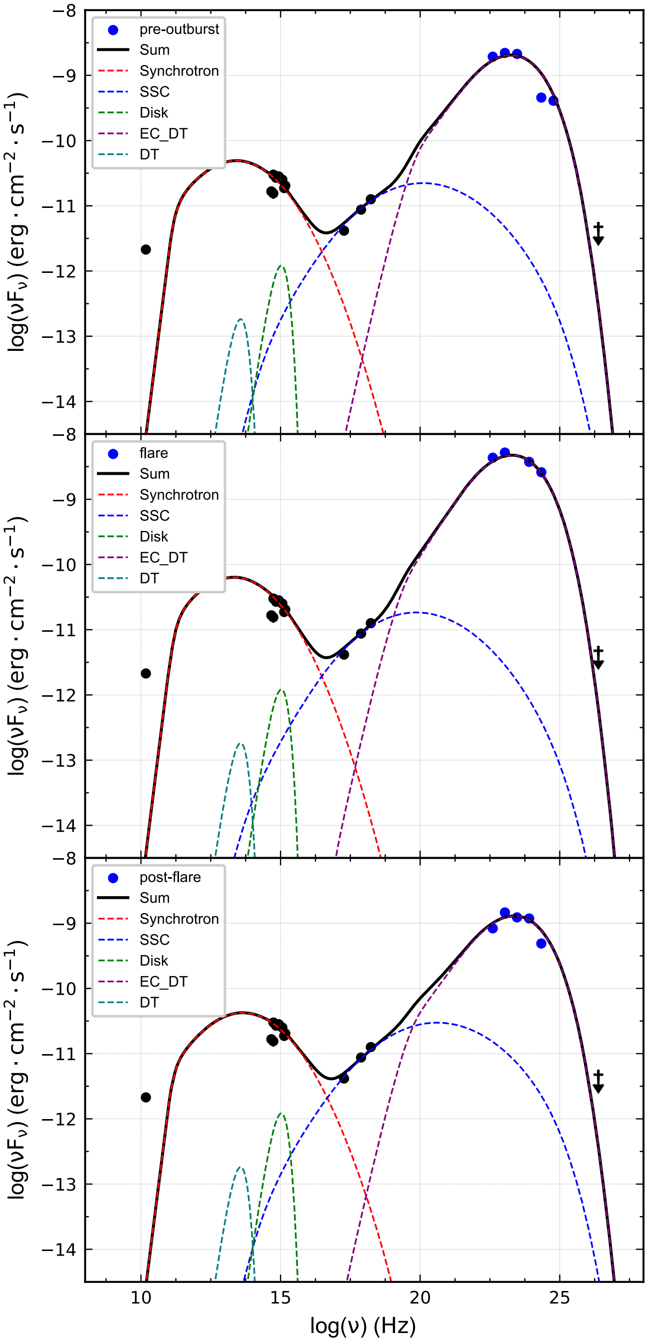

Figure 5. SEDs of the "pre-outburst," the "flare," and the "post-flare" states.

---

[7] https://jetset.readthedocs.io/en/latest/index.html

Table 2
Fixed Parameters in the Broadband SED Modeling of 3C 279 Flare F2

Parameter	Fixed Value for all States
$T_{\rm Disk}$ (K)	2×10^4
$L_{\rm Disk}$ (erg s^{-1})	2×10^{45}
$R_{\rm diss}$ (cm)	7×10^{16}
$R_{\rm H}$ (cm)	1×10^{17}
$\gamma_{\rm max}$	1×10^6
$\tau_{\rm DT}$	0.15

Table 3
Parameters in the Broadband SED Modeling of 3C 279 Flare F2

Parameter	"pre-outburst" State	"flare" State	"post-flare" State
B (G)	0.13	0.12	0.13
δ	32.3	40	28
N (cm^{-3})	230	240	250
γ_0	220	150	280
$\gamma_{\rm min}$	20	10	20
s	1.81	1.65	1.81
r	0.67	0.69	0.64

Table 4
SED Structure and Jet Power Quantities Obtained through the Modeling

Parameter	"pre-outburst" State	"flare" State	"post-flare" State
$\nu_{\rm syn}$ (Hz, log)	13.45	13.29	13.69
$\nu_{\rm IC}$ (Hz, log)	23.23	23.23	23.43
$\nu_{\rm DT}$ (Hz, log)	13.57	13.57	13.57
$P_{\rm e}$ (erg s^{-1})	9.59×10^{45}	1.09×10^{46}	8.55×10^{45}
$P_{\rm p}$ (erg s^{-1})	1.66×10^{46}	2.66×10^{46}	1.36×10^{46}
$P_{\rm B}$ (erg s^{-1})	3.23×10^{44}	4.23×10^{44}	2.43×10^{44}
$P_{\rm r}$ (erg s^{-1})	3.76×10^{45}	5.45×10^{45}	3.24×10^{45}

3.3. The Jet Kinematics

The blazar, 3C 279 at the redshift 0.536, is one of the extreme variable celestial objects in multi-wavelengths. In 2018, it demonstrated three outbursts, namely F1, F2, and F3, with GeV γ-ray fluxes exceeding the previous flare in 2015. Especially, an unprecedented high flux was observed in flare F2.

We, in particular, analyzed the spectral behavior of flare F2, which pronounced "pre-outburst," "flare" and "post-flare," seen in Figure 3. The spectral fitting results above 100 MeV are shown in Table 1. It showed clearly that a "harder-when-brighter" trend was observed for F2, which suggests the detection of a high-energy photon during the high state.

During the broadband SED modeling, we fixed parameters and used those values as in Tolamatti et al. (2022). In their work, those parameters were optimized during the fitting procedure and consistent with those values in literature (Hayashida et al. 2015; Paliya et al. 2015). In addition, we also assumed a fraction $\tau_{\rm DT} = 0.15$ of the disk luminosity was intercepted and re-radiated from dust as IR emission, as a comparison, this value was used as 0.5 for Aleksić et al. (2011) and in Paliya et al. (2015) and was used as 0.1 in Hayashida et al. (2012, 2015).

One should be able to calculate the jet power with these given fixed parameters and those parameters obtained through SED modeling. The jet power $P_{\rm jet}$, which is a critical parameter to understand the formation and composition of jets, is usually assumed to be carried by relativistic electrons ($P_{\rm e}$), magnetic field ($P_{\rm B}$), radiation ($P_{\rm r}$) and cold proton kinetic ($P_{\rm p}$) (Celotti & Ghisellini 2008; Tan et al. 2020) as:

$$P_{\rm jet} = \Sigma_i \pi R^2 \Gamma^2 c U_i, \tag{3}$$

where U_i represents the energy density of the magnetic field ($i = B$), the relativistic electron ($i = e$), cold proton ($i = p$) and bolometric radiation ($i = r$) (Ghisellini & Tavecchio 2010; Ding et al. 2019) in the comoving frame, and can be estimated in Tan et al. (2020):

$$U_{\rm e} = m_{\rm e} c^2 \int N(\gamma)\gamma d\gamma, \tag{4}$$

$$U_{\rm p} = m_{\rm p} c^2 \int 0.1 N(\gamma) d\gamma, \tag{5}$$

where we applied a standard assumption of one cold proton every ten electrons;

$$U_{\rm B} = B^2/8\pi, \tag{6}$$

$$U_{\rm r} = L_{\rm obs}/(4\pi R^2 c \delta^2), \tag{7}$$

where $L_{\rm obs}$ is the observed non-thermal bolometric luminosity, which is estimated by integrating over the broadband SED. The $P_{\rm e}$, $P_{\rm p}$, $P_{\rm B}$, $P_{\rm r}$ are calculated and tabulated in Table 3.

Our results suggest the magnetic field stays stable, but we find a slightly higher magnetic field for low activity states and a lower magnetic field for the high emission state, which has also been reported in previous works (Shah et al. 2019; Prince 2020). Besides, the Doppler factor varies and the relativistic electron distribution changed significantly during the "pre-outburst," "flare," and "post-flare" states. The Doppler factor gives the largest value for the "flare" state, while giving the smallest value for the "post-flare" state among the three states; This is consistent with the fact found in Shah et al. (2019), in which they studied the flare of 3C 279 in 2018 January and found that the bulk Lorentz factor increased when the flux increased. During the "flare" state, the electron energy distribution is significantly changed, $\gamma_{\rm min}$, γ_0, and s are becoming smaller, compared to those of the "pre-outburst" state and the "post-flare" state.

Different explanations of this flare have been purposed by previous studies. Shukla & Mannheim (2020) analyzed the

Table 5
The Magnetization Ratio and the Electron to Magnetic Field Energy Density Ratio

Parameter	"pre-outburst" State	"flare" State	"post-flare" State
σ_B	0.012	0.011	0.011
U_e/U_B	29.61	25.65	35.12

light curve of F2 and found a ∼8 minutes timescale flare, which was superimposed on a longer duration envelope, and a peak-in-peak structure in this flare. They suggested a magnetic reconnection-derived particle acceleration to form the fast flare as well as the observed peak-in-peak light curve structure. However, Tolamatti et al. (2022) suggested that the flare should not be caused by a magnetic reconnection process, because they found the jet is particle dominated ($U_e/U_B \gg 1$) and the magnetization ratio ($\sigma_B = P_B/(P_e + P_p)$) is too low to accelerate particles via magnetic reconnection, base on what they suggested the shock-in-jet may still responsible for the particle acceleration in the jet.

In analogy, we calculate the U_e/U_B and σ_B and report them in Table 5, our results suggest that the particle energy density dominates over magnetic energy density. And the low values of $\sigma_B \sim 0.01$ indicate that magnetic reconnection is less likely to account for particle acceleration, but it can accelerate electrons via relativistic shocks as suggested by Baring et al. (2017), in which electrons would be efficiently accelerated by relativistic shocks in blazar jets with σ_B ranges from $\sim 10^{-4}$ to 0.06.

Our results of Table 5 meet the conclusion from Tolamatti et al. (2022), but the contradiction between the shock acceleration in the emission blob and the minute-scale variability still exist that mentioned by Shukla & Mannheim (2020). Besides, the EED with a spectral index ∼2 predicted by the non-relativistic shock acceleration and ∼2.2 for the case of a classic relativistic shock (Baring et al. 1999; Kirk et al. 2000; Ellison & Double 2004; Hu et al. 2020), but we obtained a much harder electron spectrum with $s = 1.65$ for the flaring state.

Instead of both the shock acceleration and the magnetic reconnection, we consider this flare is possibly caused by an injection of higher-energy electrons from outside of the blob, these electrons are accelerated to higher energy outside and injected into the blob in a very short time. This injection of higher-energy electrons changes the distribution of electrons to a harder spectrum and the increases amount of electrons with energy above γ_0. These higher-energy electrons could be accelerated by a more comprehensive mechanism that can explain the unique light curve behavior (i.e., "peak-in-peak" structure), for instance, they are accelerated by the magnetic reconnection outside the blob and also obtain energy from the shock inside the blob. Otherwise, a multi-zone model should be involved to explain all these phenomenon.

3.4. The Cooling of Relativistic Electrons

In the leptonic scenario, the jet power is mostly dominated by the kinetic power of particles, including the relativistic electrons (or positrons) and cold protons. Energy dissipation of relativistic electrons is more efficient through the IC process than the synchrotron radiation resulting in a γ-ray dominant emission from the jet. The observed spectra (see in Figure 3 and Table 1) of the flare state favor a model of EC_DT, and the broadband SED has been constructed in the previous subsection. The cooling time of electrons is able to be estimated in the observer frame through

$$t_{\rm cool}^{\rm ob} = \frac{3m_e c(1+z)}{4\sigma_T \gamma \delta U'}, \tag{8}$$

where m_e is the electron rest mass, γ is the electron energy in unit of Lorentz factor, and the U' is the energy density in the jet frame. The Lorentz factor γ can be derived by the IC peak frequency: $\nu_{\rm IC} \approx \nu_{\rm ext}\gamma^2\Gamma\delta/(1+z)$, then

$$t_{\rm cool}^{\rm ob} = \frac{3m_e c}{4\sigma_T U'}\left(\frac{\nu_{\rm ext}}{\nu_{\rm IC}}\right)^{1/2}\left(\frac{\Gamma}{\delta}\right)^{1/2}(1+z)^{1/2}, \tag{9}$$

the external photon energy density $U' = 3 \times 10^{-4}\,\Gamma^2$ erg cm^{-3} and the bulk Lorentz factor (Γ) is believed to be close to the Doppler factor (δ) for blazars due to a small viewing angle (Ghisellini & Tavecchio 2008; Tavecchio et al. 2010; Foschini et al. 2011). We calculate the cooling timescale for our EC_DT model and get $t_{\rm cool}^{\rm ob} = 30.1$ minutes, 19.6 minutes, 31.8 minutes for the three states, respectively. An average cooling timescale $t_{\rm cool}^{\rm ob} = 27.2 \pm 6.6$ minutes, which meets the flux decay timescale that we obtained in the previous section (see also in Figure 2). The result suggests that the flux decay is dominated by the EC cooling of scattering DT photons and proves the dissipation region is located outside the BLR.

4. Summary

In this paper, we analyze the LAT data and investigate the rapid variability and spectral behaviors of quasar 3C 279 during the three γ-ray flares in 2018. In the obtained daily binned long-term LAT light curve, we pronounced three γ-ray flares (F1, F2, F3) during MJD 58091 to MJD 58373 in the energy range of 0.1–300 GeV. We noted that the flares F1 and F3 did not show noteworthy fast components or profiles, therefore, we only made a detailed minute timescale binned light curve and a γ-ray spectral analysis for F2. The γ-ray flux peak in F2 has exceeded the previous flare level in 2015. Then we made the broadband SED modeling, calculated the jet kinematic parameters and the cooling time of relativistic electrons, discussed the location of the γ-ray dissipation region. and came to the following conclusions:

1. Our γ-ray spectra fitting results indicate that a log-parabola model is enough to fit the spectra during the flaring state in F2. This suggests the dissipation region is outside the BLR and the energy dissipation may be due to the IC process of scattering the DT infrared photons.
2. We calculate the broadband SED for "pre-outburst," "flare," and "post-flare" states of the flare F2. We consider the EC model with soft photons origin from the DT and use the simultaneously observed multi-wavelength data from MJD 58218 to MJD 58243 for SED calculation.
3. We calculate the magnetization ratio and the electron to magnetic field energy density ratio. According to the results, we consider the flare F2 is possibly caused by an injection of higher-energy electrons from outside of the blob. Electrons are accelerated to higher energy outside and injected into the blob in a very short time.
4. Our calculation result of the cooling timescale for our EC_DT model meets the flux decay time in the LAT observation. This result suggests that the flux decay is dominated by the EC cooling of scattering DT photons, and also proves the dissipation region is located outside the BLR.

Thanks are given to the reviewer for the constructive comments and helpful suggestions. We thank Dr. A. Tolamatti for sharing the broadband SED data with us. The work is partially supported by the National Natural Science Foundation of China (NSFC U2031201, NSFC 11733001), Guangdong Major Project of Basic and Applied Basic Research (grant No. 2019B030302001).

We also acknowledge the science research grants from the China Manned Space Project with NO. CMS-CSST-2021-A06, Scientific and Technological Cooperation Projects (2020–2023) between the People's Republic of China and the Republic of Bulgaria.

ORCID iDs

Gege Wang https://orcidorg/0000-0002-8032-4640
Junhui Fan https://orcidorg/0000-0002-5929-0968
Hubing Xiao https://orcidorg/0000-0001-8244-1229
Jinting Cai https://orcidorg/0000-0002-5876-5255

References

Abdo, A. A., Ackermann, M., Ajello, M., et al. 2011, ApJL, 733, L26
Abdollahi, S., Acero, F., Ackermann, M., et al. 2020, ApJS, 247, 33
Acero, F., Ackermann, M., Ajello, M., et al. 2015, ApJS, 218, 23
Acharyya, A., Chadwick, P. M., & Brown, A. M. 2021, MNRAS, 500, 5297
Ackermann, M., Ajello, M., Atwood, W. B., et al. 2015, ApJ, 810, 14
Ackermann, M., Anantua, R., Asano, K., et al. 2016, ApJL, 824, L20
Ajello, M., Angioni, R., Axelsson, M., et al. 2020, ApJ, 892, 105
Aleksić, J., Antonelli, L. A., Antoranz, P., et al. 2011, ApJL, 730, L8
Arbeiter, C., Pohl, M., & Schlickeiser, R. 2002, A&A, 386, 415
Atwood, W. B., Abdo, A. A., Ackermann, M., et al. 2009, ApJ, 697, 1071
Baring, M. G., Böttcher, M., & Summerlin, E. J. 2017, MNRAS, 464, 4875
Baring, M. G., Ellison, D. C., Reynolds, S. P., Grenier, I. A., & Goret, P. 1999, ApJ, 513, 311
Błażejowski, M., Sikora, M., Moderski, R., & Madejski, G. M. 2000, ApJ, 545, 107
Britto, R. J., Bottacini, E., Lott, B., Razzaque, S., & Buson, S. 2016, ApJ, 830, 162
Brown, A. M. 2013, MNRAS, 431, 824
Celotti, A., & Ghisellini, G. 2008, MNRAS, 385, 283
Dermer, C. D., Finke, J. D., Krug, H., & Böttcher, M. 2009, ApJ, 692, 32
Dermer, C. D., & Schlickeiser, R. 1993, ApJ, 416, 458
Ding, N., Gu, Q. S., Geng, X. F., et al. 2019, ApJ, 881, 125
Ellison, D. C., & Double, G. P. 2004, APh, 22, 323
Fan, J.-H. 2002, PASJ, 54, L55
Fan, J.-H., Bastieri, D., Yang, J.-H., et al. 2014, RAA, 14, 1135
Fan, J. H., Kurtanidze, S. O., Liu, Y., et al. 2021, ApJS, 253, 10
Fan, Z., Cao, X., & Gu, M. 2006, ApJ, 646, 8
Fiorucci, M., Ciprini, S., & Tosti, G. 2004, A&A, 419, 25
Foschini, L., Ghisellini, G., Tavecchio, F., Bonnoli, G., & Stamerra, A. 2011, A&A, 530, A77
Ghisellini, G., Maraschi, L., & Dondi, L. 1996, A&AS, 120, 503
Ghisellini, G., & Tavecchio, F. 2008, MNRAS, 387, 1669
Ghisellini, G., & Tavecchio, F. 2009, MNRAS, 397, 985
Ghisellini, G., & Tavecchio, F. 2010, MNRAS, 409, L79
Goyal, A., Soida, M., Stawarz, Ł., et al. 2022, ApJ, 927, 214
Gupta, A. C., Agarwal, A., Bhagwan, J., et al. 2016, MNRAS, 458, 1127
Hartman, R. C., Bertsch, D. L., Fichtel, C. E., et al. 1992, ApJL, 385, L1
Hayashida, M., Madejski, G. M., Nalewajko, K., et al. 2012, ApJ, 754, 114
Hayashida, M., Nalewajko, K., Madejski, G. M., et al. 2015, ApJ, 807, 79
Hu, W., Yan, D., Dai, B., Zeng, W., & Hu, Q. 2020, MNRAS, 493, 410
Hu, W., Yan, D., & Hu, Q. 2021, MNRAS, 503, 2523
Kirk, J. G., Guthmann, A. W., Gallant, Y. A., & Achterberg, A. 2000, ApJ, 542, 235
Kirk, J. G., Rieger, F. M., & Mastichiadis, A. 1998, A&A, 333, 452
Lynds, C. R., Stockton, A. N., & Livingston, W. C. 1965, ApJ, 142, 1667
MAGIC Collaboration, Albert, J., Aliu, E., et al. Sci, 320, 1752
Massaro, E., Tramacere, A., Perri, M., Giommi, P., & Tosti, G. 2006, A&A, 448, 861
Mastichiadis, A., & Kirk, J. G. 2002, PASA, 19, 138
Nilsson, K., Pursimo, T., Villforth, C., Lindfors, E., & Takalo, L. O. 2009, A&A, 505, 601
Paliya, V. S., Sahayanathan, S., & Stalin, C. S. 2015, ApJ, 803, 15
Poutanen, J., & Stern, B. 2010, ApJL, 717, L118
Prince, R. 2020, ApJ, 890, 164
Shah, Z., Jithesh, V., Sahayanathan, S., Misra, R., & Iqbal, N. 2019, MNRAS, 484, 3168
Shukla, A., & Mannheim, K. 2020, NatCo, 11, 4176
Shukla, A., Mannheim, K., Patel, S. R., et al. 2018, ApJL, 854, L26
Sikora, M., Begelman, M. C., & Rees, M. J. 1994, ApJ, 421, 153
Sokolov, A., & Marscher, A. P. 2005, ApJ, 629, 52
Tan, C., Xue, R., Du, L.-M., et al. 2020, ApJS, 248, 27
Tanaka, Y. T., Stawarz, Ł., Thompson, D. J., et al. 2011, ApJ, 733, 19
Tavecchio, F., Ghisellini, G., Bonnoli, G., & Ghirlanda, G. 2010, MNRAS, 405, L94
Tavecchio, F., Maraschi, L., & Ghisellini, G. 1998, ApJ, 509, 608
Tolamatti, A., Ghosal, B., Singh, K. K., et al. 2022, APh, 139, 102687
Tramacere, A. 2020, JetSeT: Numerical Modeling and SED Fitting Tool for Relativistic Jets, Astrophysics Source Code Library, ascl:2009.001
Tramacere, A., Giommi, P., Perri, M., Verrecchia, F., & Tosti, G. 2009, A&A, 501, 879
Tramacere, A., Massaro, E., & Taylor, A. M. 2011, ApJ, 739, 66
Urry, C. M., & Padovani, P. 1995, PASP, 107, 803
Villata, M., Raiteri, C. M., Balonek, T. J., et al. 2006, A&A, 453, 817
Wills, B. J., Wills, D., Breger, M., Antonucci, R. R. J., & Barvainis, R. 1992, ApJ, 398, 454
Xiao, H., Fan, J., Yang, J., et al. 2019, SCPMA, 62, 129811
Xiao, H. B., Pei, Z. Y., Xie, H. J., et al. 2015, Ap&SS, 359, 39
Yang, W. X., Wang, H. G., Liu, Y., et al. 2022, ApJ, 925, 120